Electronic Supplementary Material (ESI) for Inorganic Chemistry Frontiers.

Supporting information for

Smart intercalation collaborating coordination strategy to construct stable ratiometric fluorescence nanoprobe for detection of anthrax biomarker

Xiaoxiao Niu, Meixiang Wang, Mengyu Zhang, Rui Cao, Zhaodi Liu*, Fuying Hao, Liangquan Sheng and Huajie Xu*

Supplementary Figures:

DPA.

Fig. S19. Time-resolved decay curves of L@Mg-Al-Tb-LDHs and L@Mg-Al-Eu-LDHs before and after the addition of DPA.

Fig. S20. Photographs of L@Mg-Al-Eu-LDHs with and without DPA under 254nm UV light.

Fig. S21. Plot of fluorescence intensity ratio (I_{545}/I_{464}) versus DPA concentration.

Fig. S22. Plot of fluorescence intensity ratio (I_{615}/I_{464}) versus DPA concentration.

Fig. S23. The dependence of the I_{545}/I_{464} ratio of the L@Mg-Al-Tb-LDHs nanoprobe and the I_{615}/I_{464} ratio of the L@Mg-Al-Eu-LDHs nanoprobe on pH, respectively.

Fig. S24. Fluorescence of L@Mg-Al-Eu-LDHs equipped portable test strips for DPA detection, and plot of G/B (R/B) ratio versus C_{DPA} (μM).

Fig. S25. Fluorescence spectra of L@Mg-Al-Eu-LDHs on different volumes of B. subtilis spores, and the plot of fluorescence intensity at I_{615}/I_{464} against the concentration of DPA concentration released by B. subtilis.

Fig. S26. Fluorescence emission spectra of L@Mg-Al-Eu-LDHs with different concentrations of DPA in 10% bovine serum, and the plot of fluorescence intensity at I_{615}/I_{464} against the concentration of DPA.

Supplementary Tables：

Table S1. The weight percentage content of elements in L@Mg-Al-Ln-LDHs from ICP-AES and elemental analysis data.

Table S2. Fluorescence decay lifetime parameters of L@Mg-Al-Tb-LDHs (545 nm) and L@Mg-Al-Eu-LDHs (615 nm).

Table S3. Comparison of some reported probes on DPA detection.

Table S4. Results of the analysis of Bacillus subtilis spores in real samples using L@Mg-Al-Tb-LDHs and L@Mg-Al-Eu-LDHs.

Table S5. RSD datas for the relative intensities of L@Mg-Al-Tb-LDHs (I_{545}/I_{464}) and L@Mg-Al-Eu-LDHs (I_{615}/I_{464}) in 10% bovine serum.

Reference

Supplementary Figures

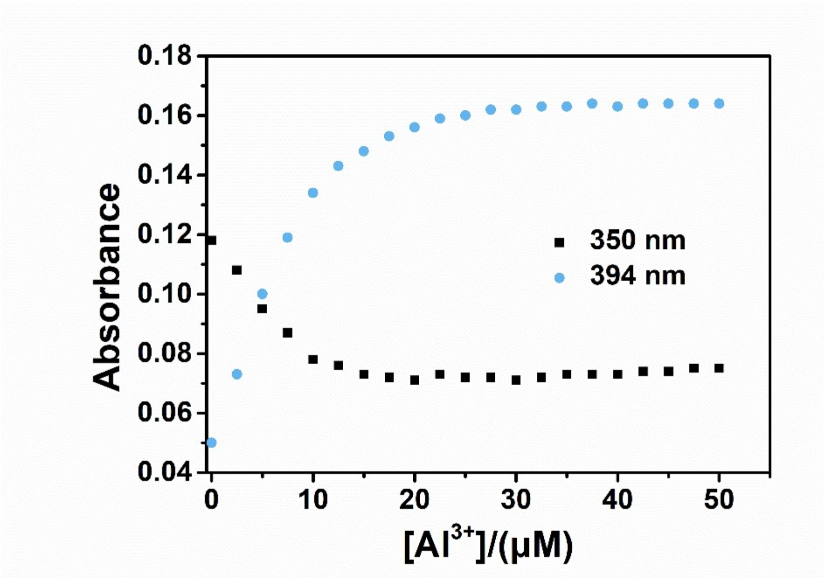

Fig. S1. Absorbance at 350 nm and 394 nm of L as a function of Al^{3+} concentration.

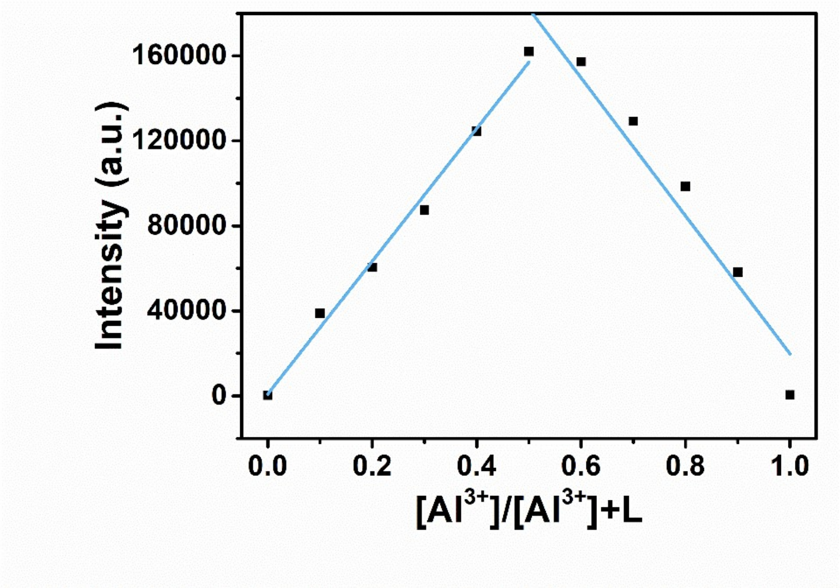

Fig. S2. Job's plots according to the method for continuous variations. The total concentration of L and Al^{3+} is 100 μM.

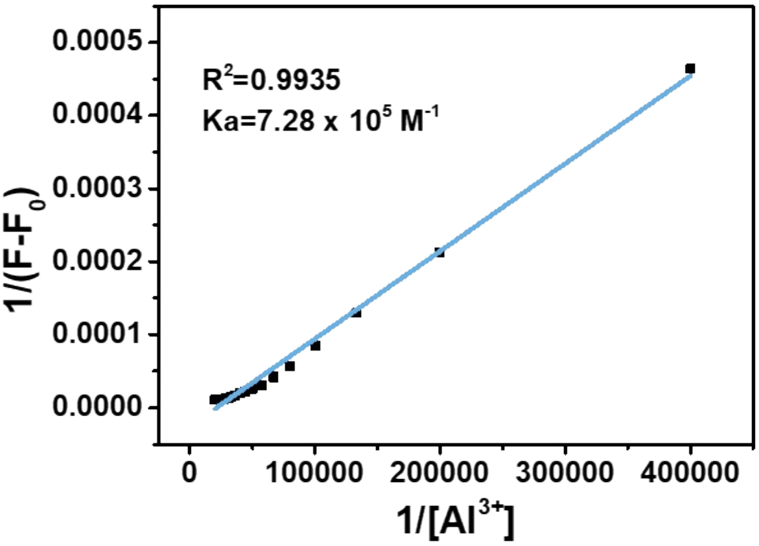

Fig. S3. Benesi–Hildebrand plot of L with Al^{3+} in Tris-HCl buffer solutions (pH=7.5, 10.0 mM).

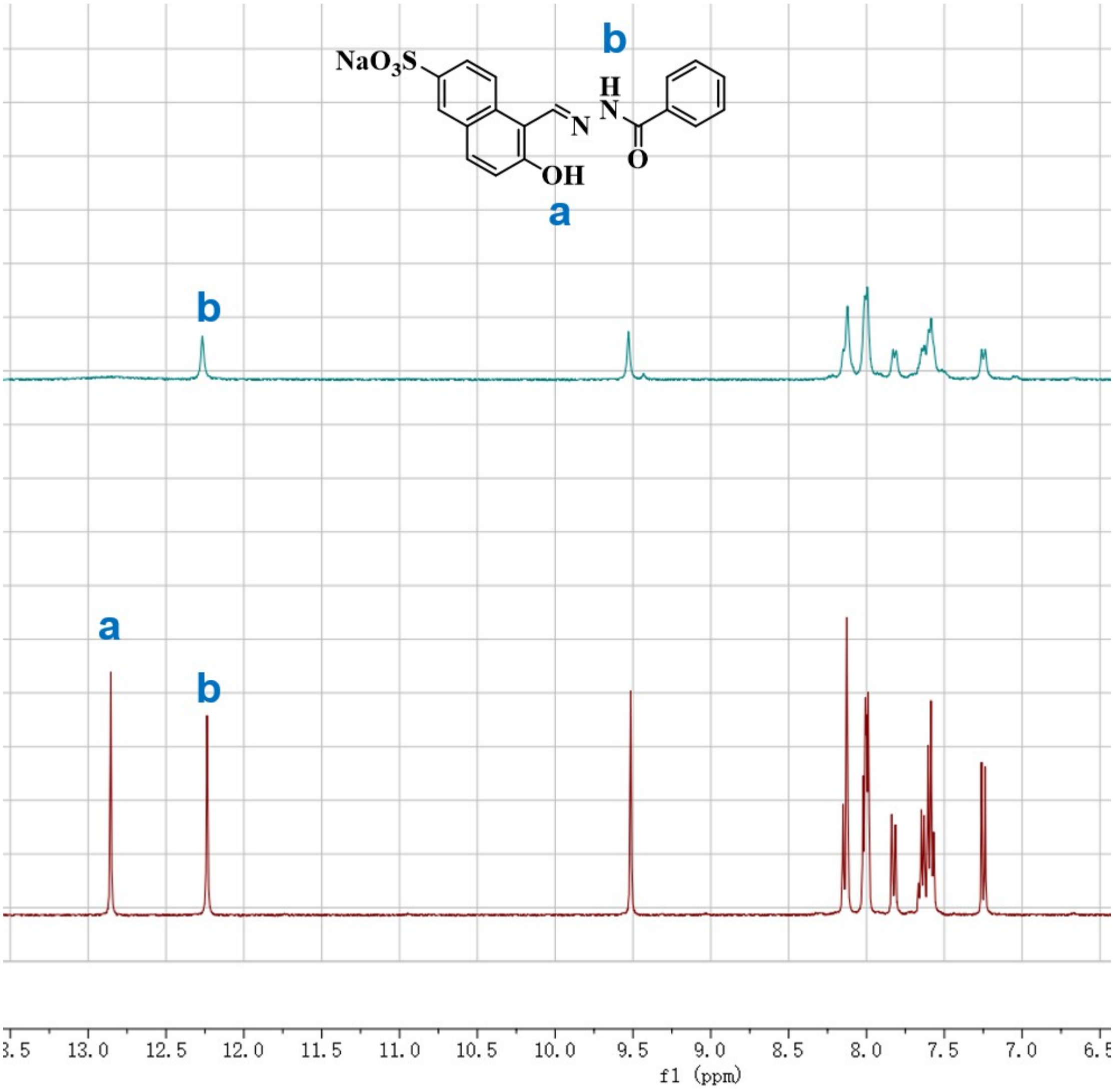

Fig. S4. ^{1}HNMR titrations of L and L alone with Al^{3+} ions in DMSO-*d*6.

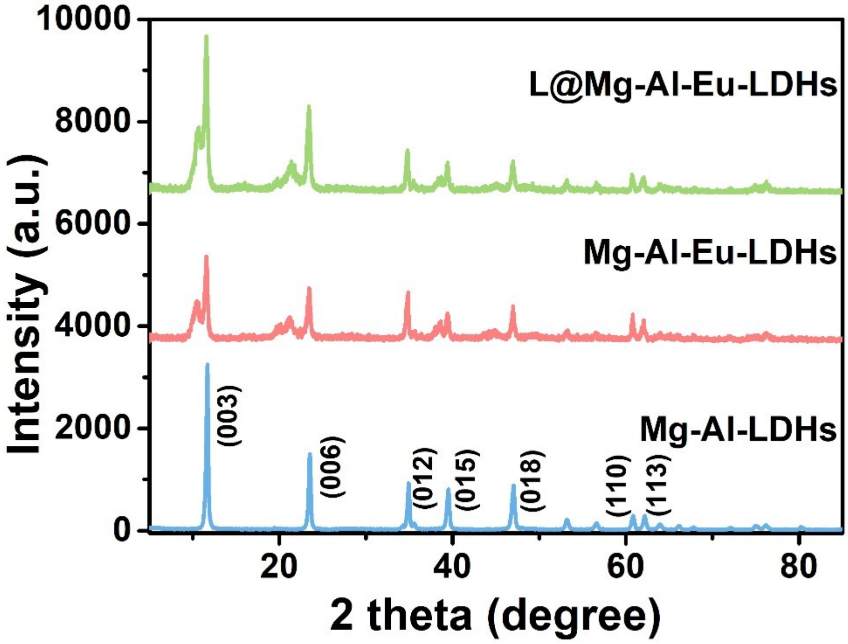

Fig. S5. XRD patterns of Mg-Al-LDHs, Mg-Al-Eu-LDHs and L@Mg-Al-Eu-LDHs.

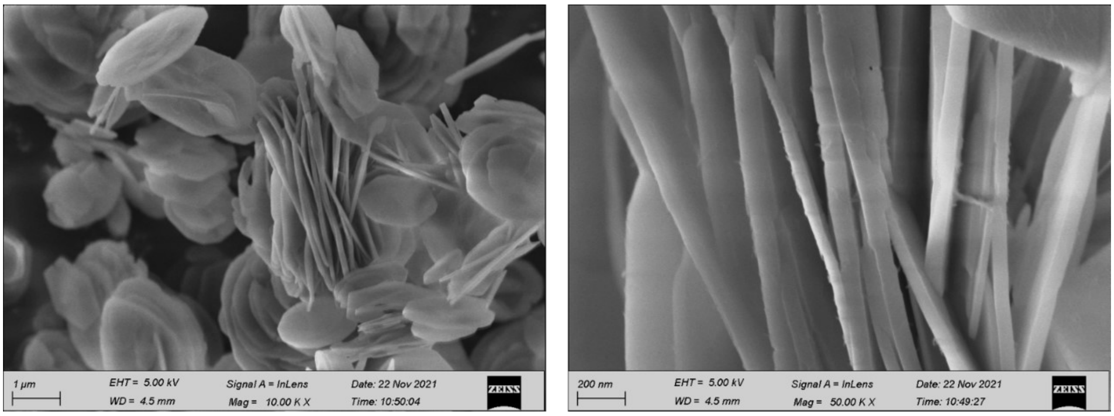

Fig. S6. SEM images of Mg-Al-LDHs.

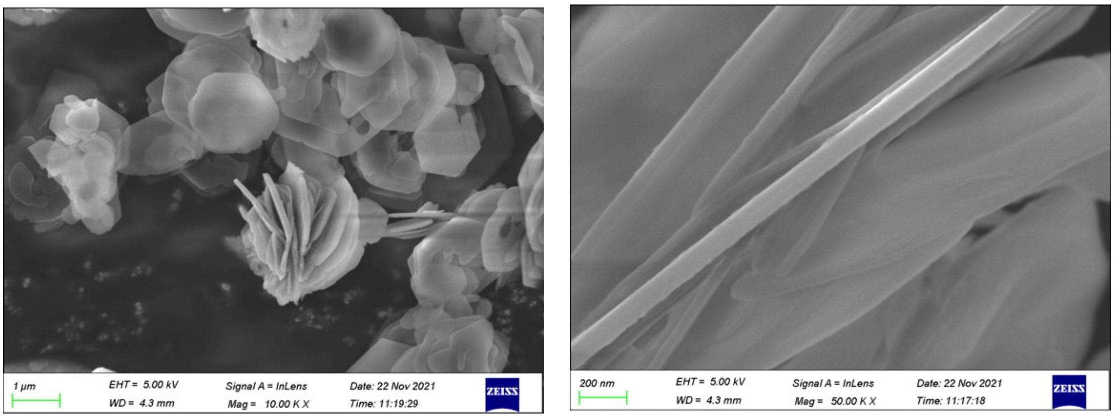

Fig. S7. SEM images of Mg-Al-Eu-LDHs.

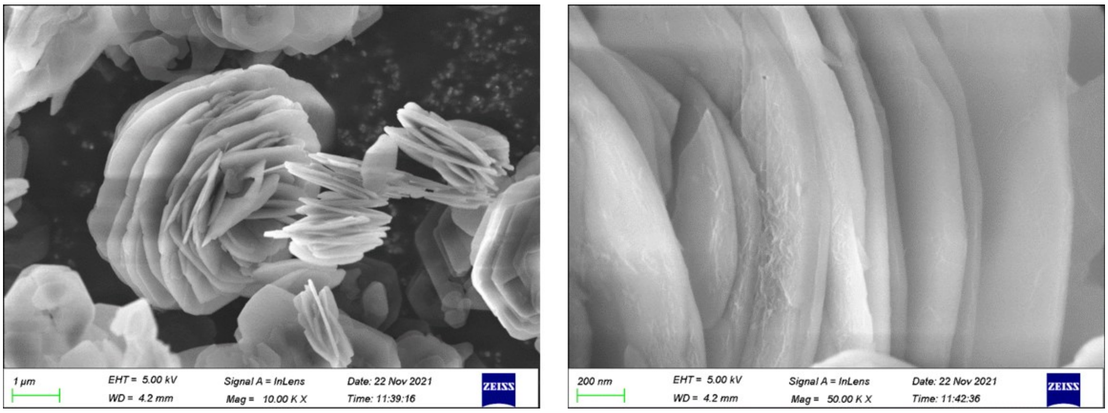

Fig. S8. SEM images of L@Mg-Al-Eu-LDHs.

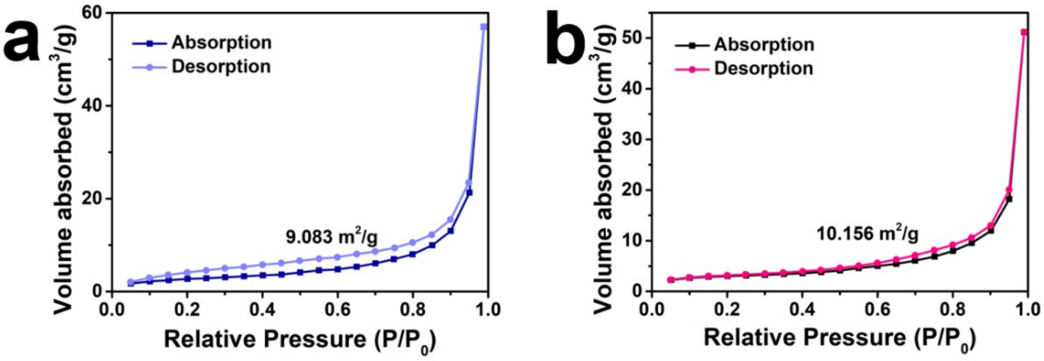

Fig. S9. N_2 sorption isotherms and pore-size distribution of (a) L@Mg-Al-Tb-LDHs and (b) L@Mg-Al-Eu-LDHs.

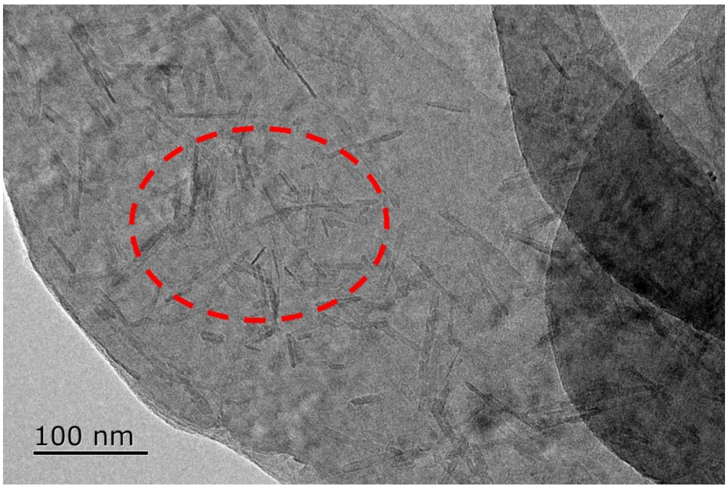

Fig. S10. TEM images of L@Mg-Al-Eu-LDHs.

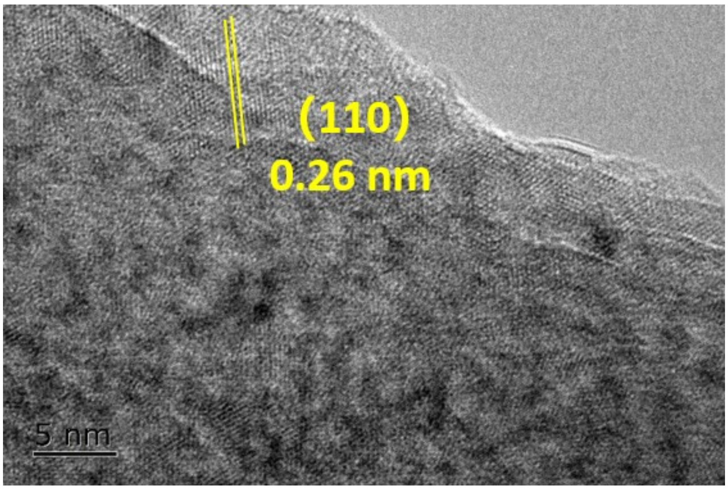

Fig. S11. HRTEM images of L@Mg-Al-Eu-LDHs.

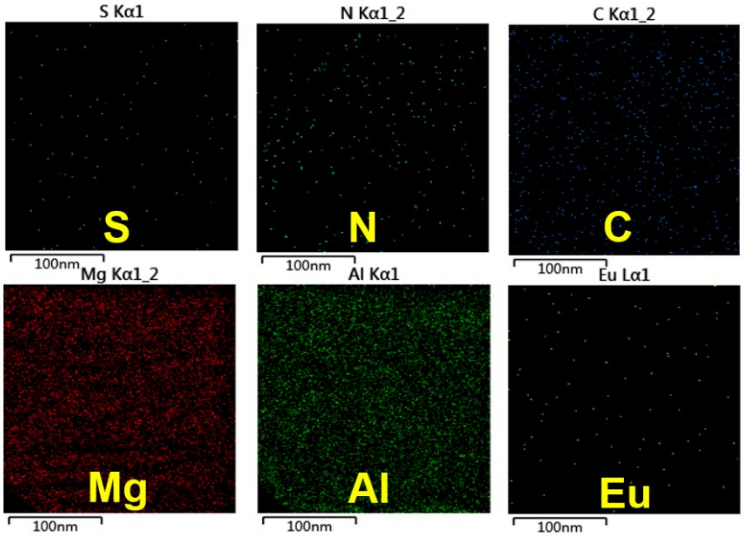

Fig. S12. Elemental mapping images of L@Mg-Al-Eu-LDHs.

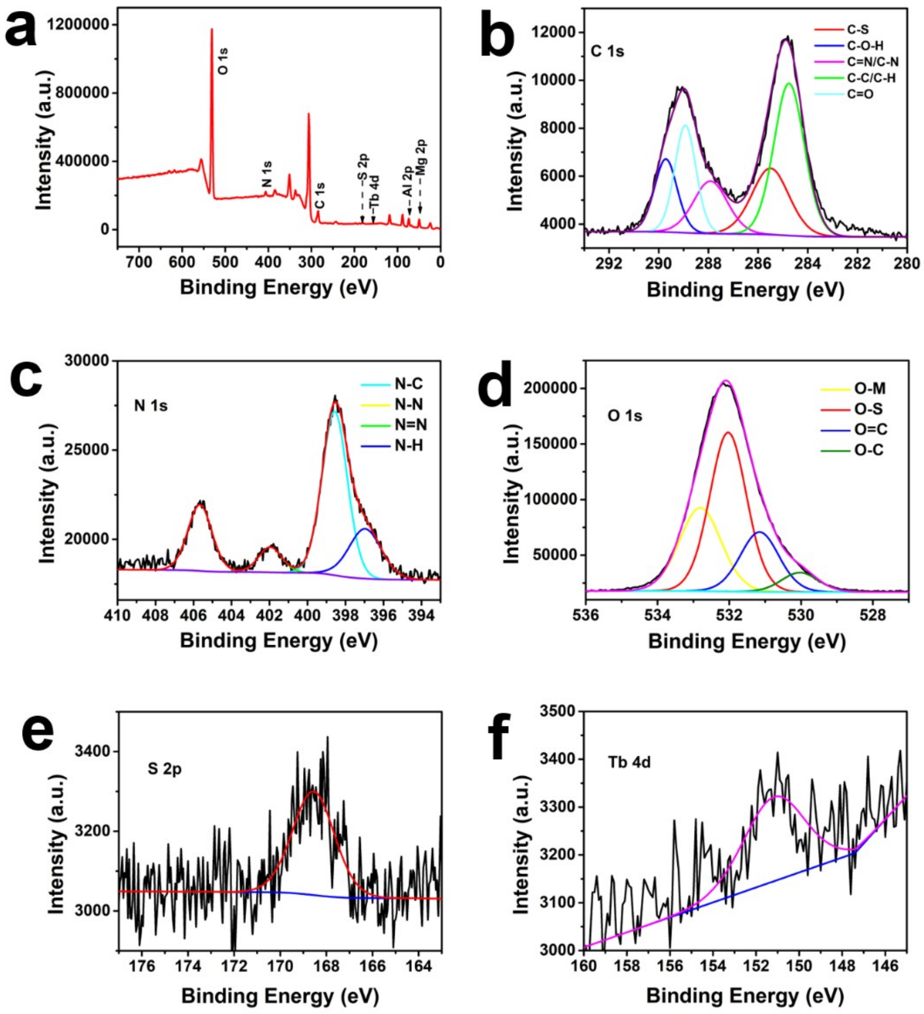

Fig. S13. XPS spectrum of L@Mg-Al-Tb-LDHs.

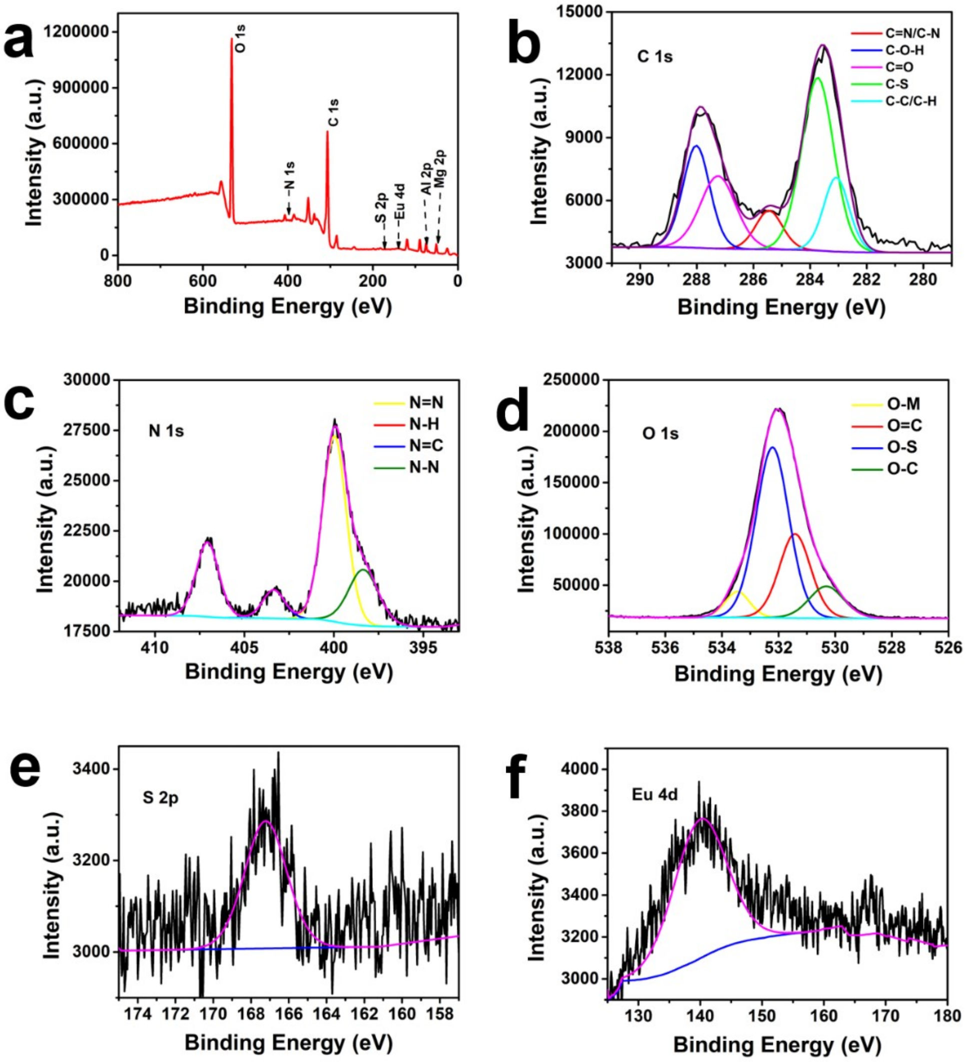

Fig. S14. XPS spectrum of L@Mg-Al-Eu-LDHs.

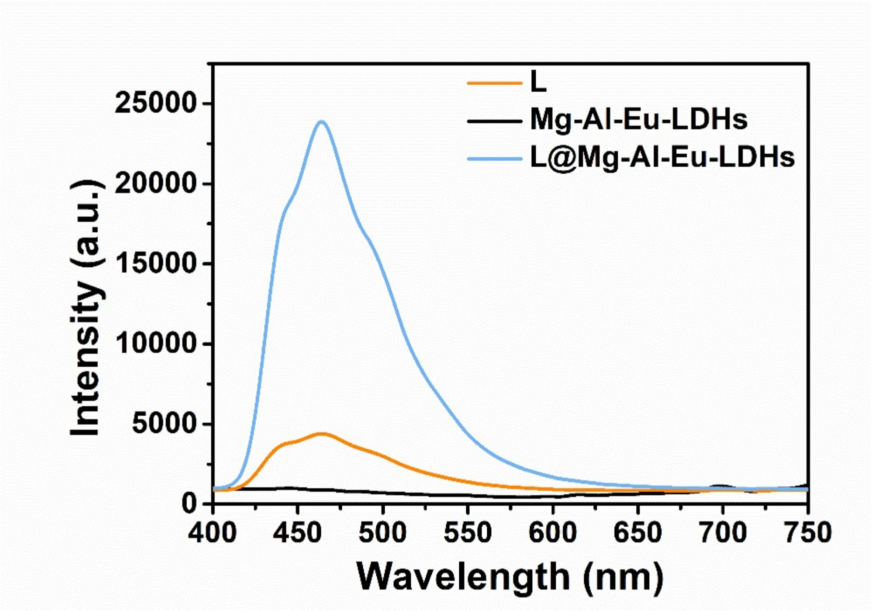

Fig. S15. Fluorescence spectra of L, Mg-Al-Eu-LDHs and L@Mg-Al-Eu-LDHs.

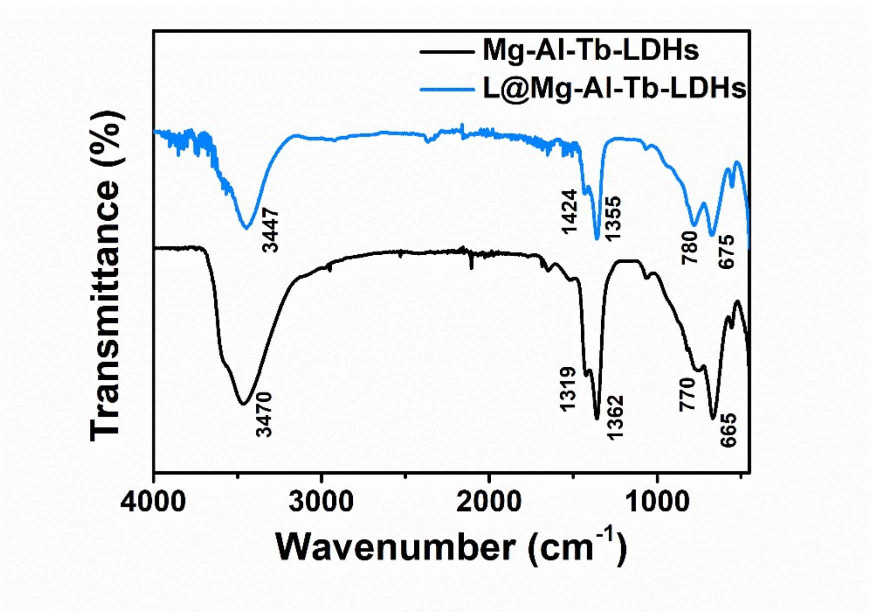

Fig. S16. FTIR spectra of Mg-Al-Tb-LDHs and L@Mg-Al-Tb-LDHs.

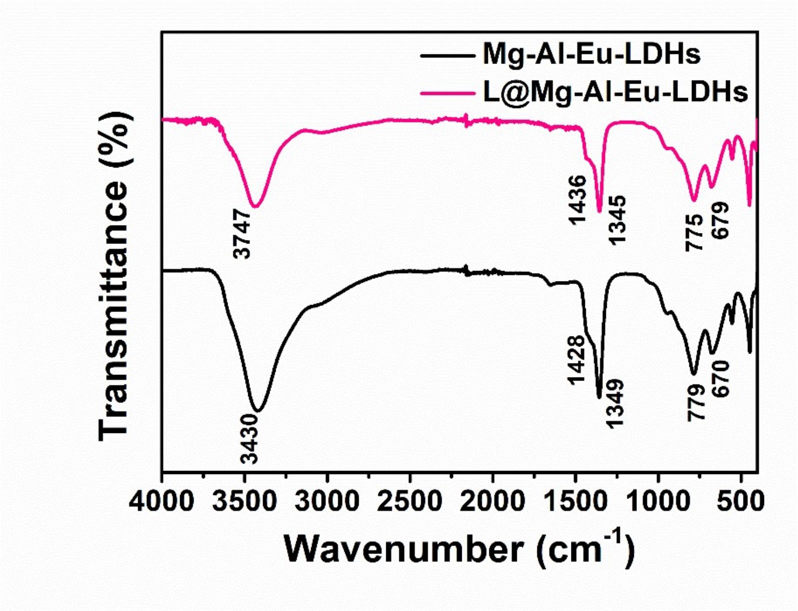

Fig. S17. FTIR spectra of Mg-Al-Eu-LDHs and L@Mg-Al-Eu-LDHs.

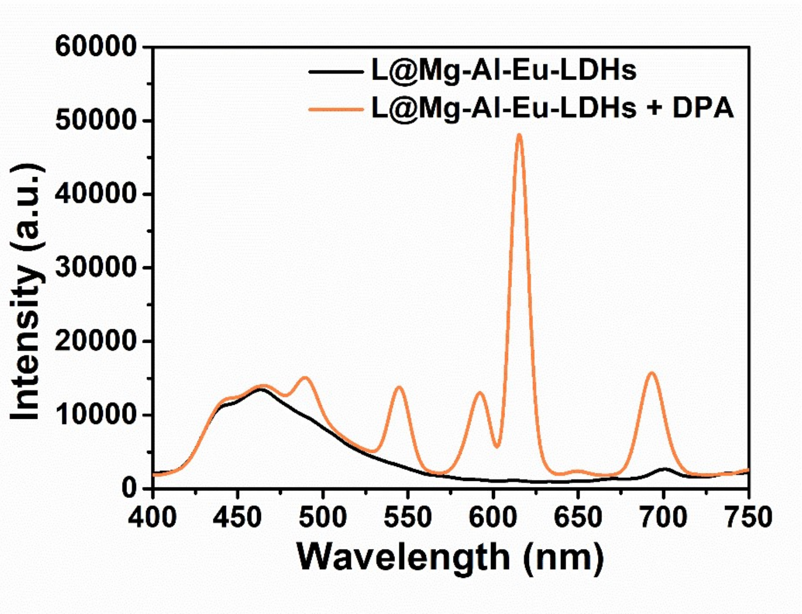

Fig. S18. Fluorescence spectra of L@Mg-Al-Eu-LDHs and L@Mg-Al-Eu-LDHs + DPA.

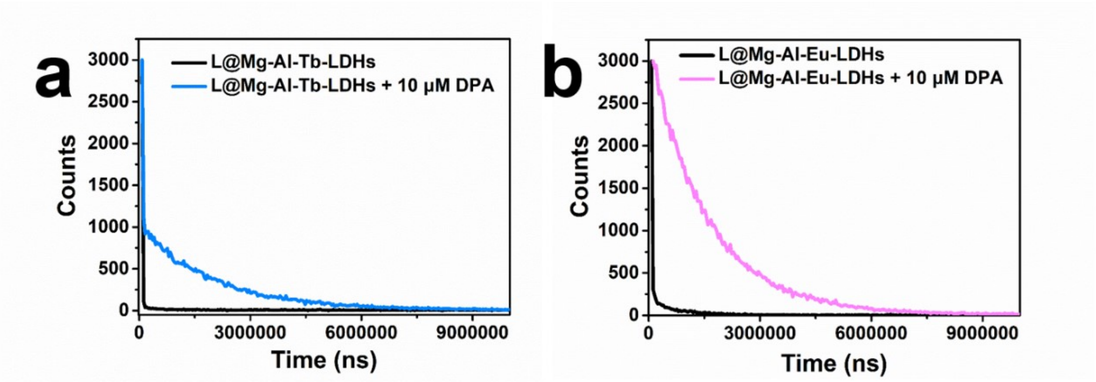

Fig. S19. (a) Time-resolved decay curves of L@Mg-Al-Tb-LDHs before and after the addition of DPA, λ_{ex}=275 nm and λ_{em}=545 nm. (b) Time-resolved decay curves of L@Mg-Al-Eu-LDHs before and after the addition of DPA, λ_{ex}=275 nm and λ_{em}=615 nm.

Fig. S20. Photographs of L@Mg-Al-Eu-LDHs with and without DPA under 254 nm UV light.

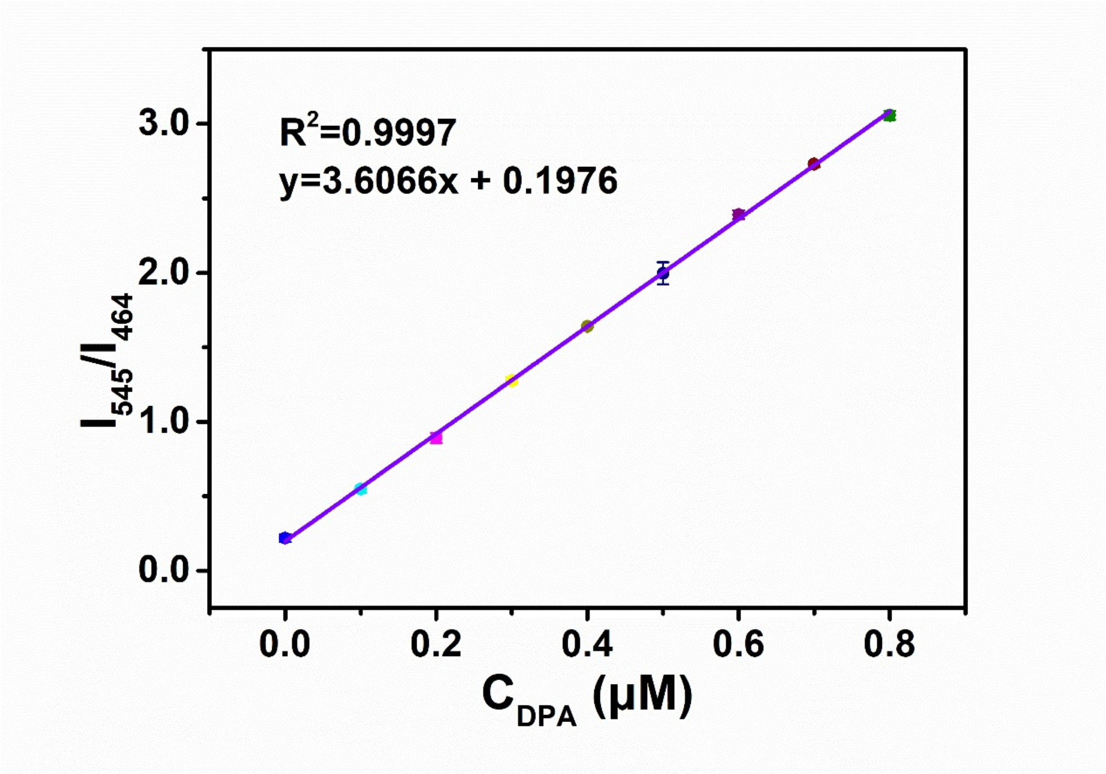

Fig. S21. Plot of fluorescence intensity ratio (I_{545}/I_{464}) versus DPA concentration.

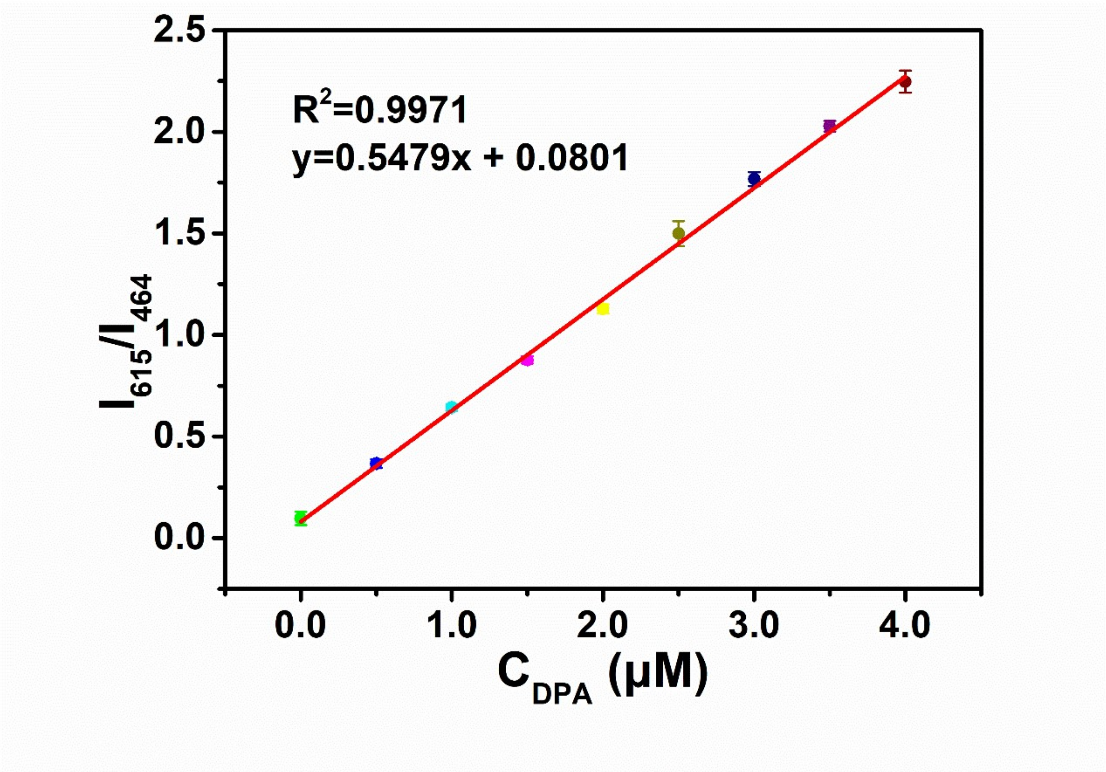

Fig. S22. Plot of fluorescence intensity ratio (I_{615}/I_{464}) versus DPA concentration.

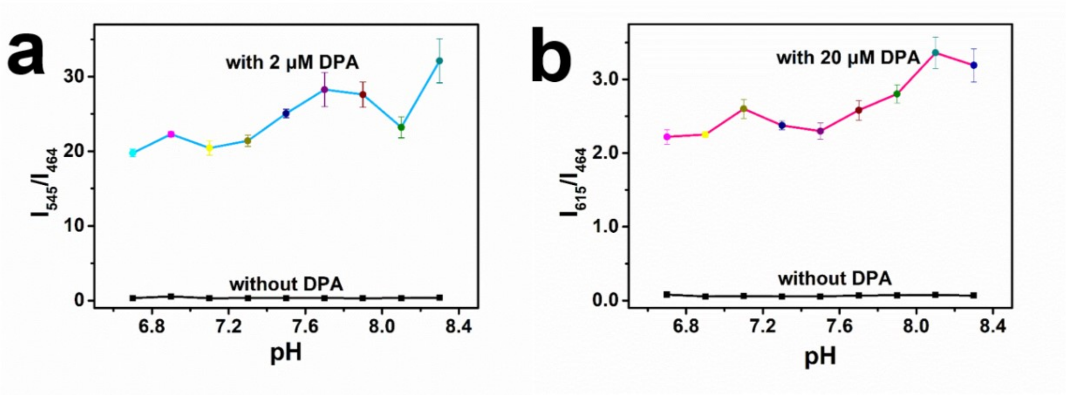

Fig. S23. (a) The dependence of I_{545}/I_{464} ratio of the L@Mg-Al-Tb-LDHs nanoprobe with pH (pH=6.7-8.4). (b) The dependence of I_{615}/I_{464} ratio of the L@Mg-Al-Eu-LDHs nanoprobe with pH (pH=6.7-8.4).

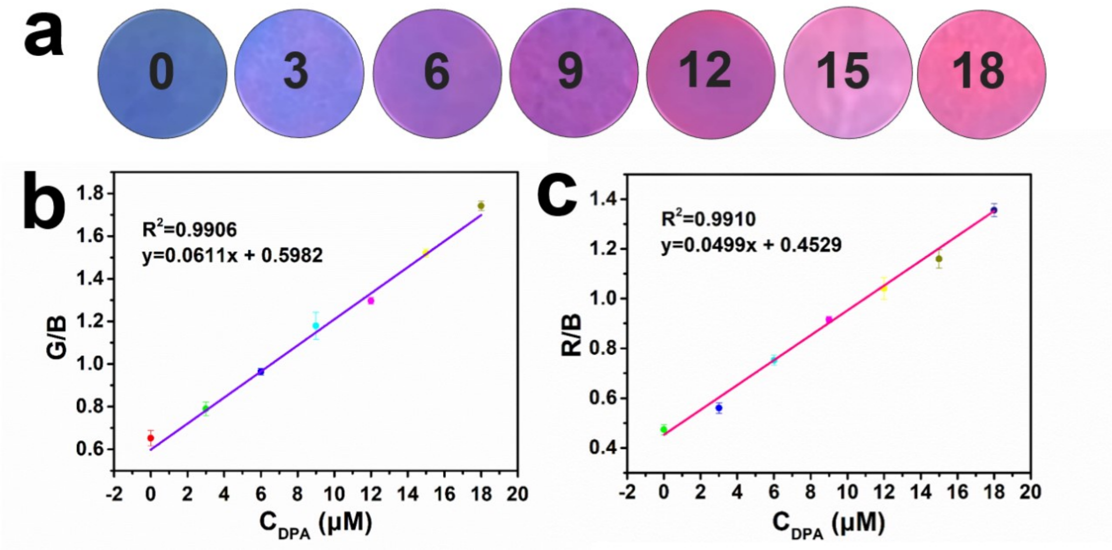

Fig. S24. (a) Fluorescence of L@Mg-Al-Eu-LDHs equipped portable test strips for DPA detection (0-18 μM) . (b) Plot of G/B ratio versus C_{DPA} (μM). Error bars indicate standard deviations. (c) Plot of R/B ratio versus C_{DPA} (μM).

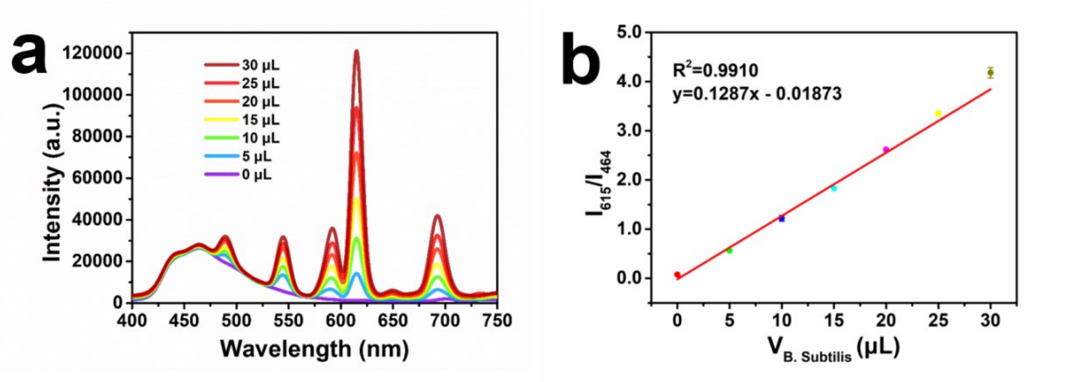

Fig. S25. (a) Fluorescence spectra of L@Mg-Al-Eu-LDHs on different volumes of B. subtilis spores (0, 5, 10, 15, 20, 25, 30 μL). (b) The plot of fluorescence intensity at I_{615}/I_{464} against the concentration of DPA concentration released by B. subtilis.

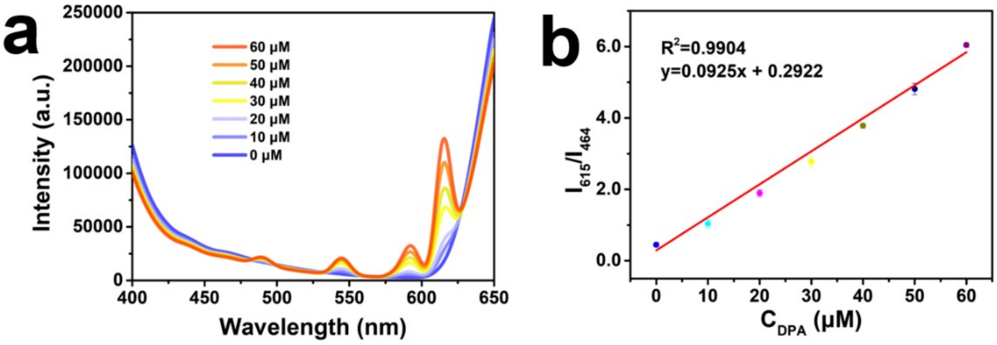

Fig. S26. (a) Fluorescence emission spectra of L@Mg-Al-Eu-LDHs with different concentrations of DPA in 10% bovine serum. (b) The plot of fluorescence intensity at I_{615}/I_{464} against the concentration of DPA from 0 to 60 μM (0, 10, 20, 30, 40, 50, 60 μM).

Supplementary Tables

Table S1. The weight percentage content of elements in L@Mg-Al-Ln-LDHs from ICP-AES and elemental analysis data.

Element	**Mg (wt%)**	**Al (wt%)**	**Tb (wt%)**	**Eu (wt%)**
L@Mg-Al-Tb-LDHs	16.74	9.87	0.65	
L@Mg-Al-Eu-LDHs	16.12	10.119		0.43

Table S2. Fluorescence decay lifetime parameters of L@Mg-Al-Tb-LDHs (545 nm) and L@Mg-Al-Eu-LDHs (615 nm).

Sensors	**DPA Concentration (μM)**	**τ_1 （μs）**	**τ_2 （μs）**	**τ_{ave} （μs）**
L@Mg-Al-Tb-LDHs	**0**	**11.76**	**11.76**	**2.35**
	10	**14.61**	**1953.63**	**432.82**
L@Mg-Al-Eu-LDHs	**0**	**618.30**	**12.75**	**17.18**
	10	**1534.01**	**1534.00**	**1530.68**

Table S3. Comparison of some reported probes on DPA detection.

Sensing material	Linear range	LOD	Ref.
Eu/Tb SAH	0-3.0 μM 0-2.4 μM	27.3 nM 1.06 nM	[1]
CDs-Tb	0-6 μM	35.9 nM	[2]
TPE-Tbs	0-18 nM	0.187 nM	[3]
TbP-CPs	0-8 μM	5.0 nM	[4]
Tb-g-C_3N_4NS	0-15 μM	9.9 nM	[5]
hPEI-CD-EDTA-Eu^{3+}	1.0-100 nM	0.19 nM	[6]
EBT-CDs@Eu	0.1-12 μM	10.6 nM	[7]
Eu@SiNPs	0-20 μM	0.15 μM	[8]
GSH-Cu NCs/Eu^{3+}	0-20 μM	8 nM	[9]
$Tb_{0.875}Eu_{0.125}$-Hddb	0-100 μM	0.8494 μM	[10]
L@Mg-Al-Tb-LDHs **L@Mg-Al-Eu-LDHs**	0-0.8 μM 0-4.0 μM	11.6 nM 27.3 nM	This work

Table S4. Results of the analysis of Bacillus subtilis spores in real samples using L@Mg-Al-Tb-LDHs and L@Mg-Al-Eu-LDHs (n=3).

Sensors	Spores added	Detected	Recovery (%, n=3)	RSD (%, n=3)
L@Mg-Al-Tb-LDHs	**0**	**Not detected**		
	1.000×10^6	**1.026×10^6**	**102.59**	**0.74**
	2.000×10^6	**1.959×10^6**	**97.95**	**0.71**
	3.000×10^6	**2.872×10^6**	**95.74**	**0.17**
	4.000×10^6	**3.740×10^6**	**93.49**	**1.23**
	5.000×10^6	**4.731×10^6**	**94.61**	**2.55**
	6.000×10^6	**5.686×10^6**	**94.76**	**2.09**
L@Mg-Al-Eu-LDHs	**0**	**Not detected**		
	1.000×10^6	**1.081×10^6**	**108.13**	**0.37**
	2.000×10^6	**2.002×10^6**	**100.11**	**0.99**
	3.000×10^6	**2.904×10^6**	**96.79**	**1.28**
	4.000×10^6	**3.883×10^6**	**97.08**	**1.27**
	5.000×10^6	**4.751×10^6**	**95.02**	**3.34**
	6.000×10^6	**5.587×10^6**	**93.11**	**1.51**

Table S5. RSD datas (n=3) for the relative intensities of L@Mg-Al-Tb-LDHs (I_{545}/I_{464}) and L@Mg-Al-Eu-LDHs (I_{615}/I_{464}) in 10% bovine serum.

Sample	DPA added (μM)	Detected (μM)	Recovery (%, n=3)	RSD (%, n=3)
L@Mg-Al-Tb-LDHs	0	Not detected		
	1.00	1.0210	99.88	0.74
	2.00	1.9820	95.27	0.71
	3.00	2.9129	103.99	0.17
	4.00	3.8859	105.76	1.22
	5.00	4.8108	104.50	2.54
	6.00	5.8378	109.72	2.09
L@Mg-Al-Eu-LDHs	0	Not detected		
	10.00	10.345	103.45	0.37
	20.00	19.466	97.33	0.99
	30.00	28.272	94.24	1.28
	40.00	38.864	97.16	1.27
	50.00	47.465	94.93	3.34
	60.00	62.634	104.39	1.51

Reference

1. P. Su, X. Wang, T. Wang, X. Feng, M. Zhang, L. Liang, J. Cao, W. Liu and Y. Tang, Eu(3+)/Tb(3+) supramolecular assembly hybrids for ultrasensitive and ratiometric detection of anthrax spore biomarker in water solution and actual spore samples, *Talanta*, 2021, **225**, 122063.
2. L. Zhang, Z. Wang, J. Zhang, C. Shi, X. Sun, D. Zhao and B. Liu, Terbium Functionalized Schizochytrium-Derived Carbon Dots for Ratiometric Fluorescence Determination of the Anthrax Biomarker, *Nanomaterials (Basel)*, 2019, **9**, 1234.
3. P. Su, L. Liang, T. Wang, P. Zhou, J. Cao, W.-S. Liu and Y. Tang, AIE-based Tb^{3+} complex self-assembled nanoprobe for ratiometric fluorescence detection of anthrax spore biomarker in water solution and actual spore samples, *Chemical Engineering Journal*, 2021, **413**, 127408.
4. Y. Luo, L. Zhang, L. Zhang, B. Yu, Y. Wang and W. Zhang, Multiporous Terbium Phosphonate Coordination Polymer Microspheres as Fluorescent Probes for Trace Anthrax Biomarker Detection, *ACS Appl Mater Interfaces*, 2019, **11**, 15998-16005.
5. Y. Y. Ma, Z. J. Wang and D. J. Qian, Ratiometric fluorescence detection of anthrax biomarker based on terbium (III) functionalized graphitic carbon nitride nanosheets, *Talanta*, 2021, **230**, 122311.
6. H. Yang, F. Lu, X. Zhan, M. Tian, Z. Yuan and C. Lu, A Eu(3+)-inspired fluorescent carbon nanodot probe for the sensitive visualization of anthrax biomarker by integrating EDTA chelation, *Talanta*, 2020, **208**, 120368.
7. Q. Zhou, Y. Fang, J. Li, D. Hong, P. Zhu, S. Chen and K. Tan, A design strategy of dual-ratiomentric optical probe based on europium-doped carbon dots for colorimetric and fluorescent visual detection of anthrax biomarker, *Talanta*, 2021, **222**, 121548.
8. M. Na, S. Zhang, J. Liu, S. Ma, Y. Han, Y. Wang, Y. He, H. Chen and X. Chen, Determination of pathogenic bacteria-Bacillus anthrax spores in environmental samples by ratiometric fluorescence and test paper based on dual-emission fluorescent silicon nanoparticles, *J Hazard Mater*, 2020, **386**, 121956.
9. J. Zhao, Y. Chen, P. Du, J. Li, Z. Zhang and X. Lu, Portable smartphone platform integrated with fluorescent test strip based on Eu^{3+}-functionalized copper nanoclusters for on-site visual recognition of a pathogenic biomarker, *Sensors and Actuators B: Chemical*, 2021, **332**, 127918.
10. X.-B. Chen, C.-X. Qi, Y.-B. Xu, H. Li, L. Xu and B. Liu, A quantitative ratiometric fluorescent Hddb-based MOF sensor and its on-site detection of the anthrax biomarker 2,6-dipicolinic acid, *Journal of Materials Chemistry C*, 2020, **8**, 17325-17335.